

# Comprehensive Modeling of Fault Dynamics During the Seismic Cycle

K. Tuncay

Faculty of Earth Sciences, Utrecht University, Netherlands

F. Renard

LGIT, Université Joseph Fourier, France

P. Ortoleva

Laboratory for Computational Geodynamics, Indiana University, USA

**ABSTRACT:** A three dimensional finite element fault model that accounts for an incremental stress rheology, and fluid and heat flow is presented. In the model, mass and momentum balances for solid and fluid phases, and a total energy conservation equation are solved numerically along with a state and rate dependent friction law at the fault surface. The model allows one to study the effect of frictional heating, fluid influx from the deeper parts of faults, effect of heterogeneities on the fault behavior at the crustal scale.

## 1 INTRODUCTION

Geological evidence indicates that, in addition to the stress state and the temperature field, fluids play a key role during the seismic cycle (Hickman *et al.* 1995). After an earthquake, fractures open in the fault and in the surroundings rocks. During the interseismic period, the permeability of the fault and the country rocks tend to decrease by gouge compaction and fracture sealing. As geologic evidence is gathered on the involvement of fluids in faults dynamics, a growing number of researchers have started to study the origins and the effects of fluid pressure variations on fault mechanics (Byerlee 1990, Rice 1992, Segall and Rice 1995, Tuncay *et al.* 2001).

The goal of this study is to demonstrate how fault dynamics can be analyzed in the context of comprehensive 3D modeling at the crustal scale. We consider a rock body sliding past a rigid plate (Fig. 1). This domain represents the volume of a tectonic plate affected by a preexisting fault on its side. Our model consists of conservation of mass, momentum, and energy equations, as well as a deformation model that accounts for many deformation mechanisms, and textural evolution.

A direct coupling of mechanics and chemistry arises through pressure solution. Grain dissolution at stressed grain-grain contacts induces compaction and, thereby, contributes to overall deformation (Renard *et al.* 2000). Another coupling arises through fracture dynamics: fractures open during a seismic event whereas fracture healing contributes to the decrease of permeability during the interseismic period. The dynamics of the fracture network is based on a statistical representation (Tuncay *et al.*

2000a). Integration of different deformation mechanisms is achieved by an incremental stress rheology (Tuncay *et al.* 2000b).

In our model we use a rate and state dependent friction law (Dieterich 1979, Ruina 1983). In this approach friction depends on velocity as well as a state variable that evolves in time. The coefficients in the friction law indicate whether the behavior is velocity weakening or strengthening. There are a number of studies that coupled this type of friction law with small strain elasticity (Tse & Rice 1986, Rice 1993). However these studies are limited to homogeneous systems and they do not account for important processes such as fluid flow, heat flow, etc.

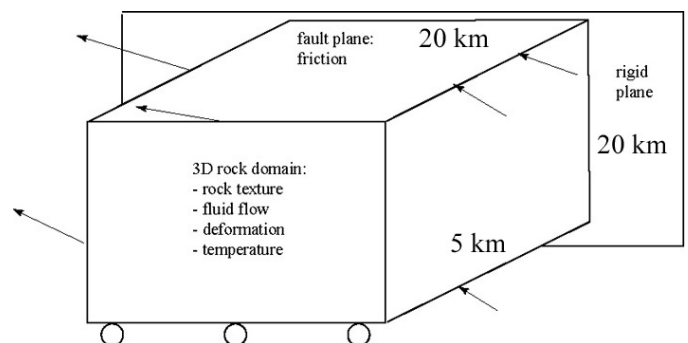


Figure 1. Schematic view of a deformable block sliding on a rigid plane. At the right-lateral slip fault plane, a state and rate dependent friction law is imposed. No vertical displacement and tangential traction are allowed at the bottom boundary. The top boundary is assumed to be traction free. The velocity field is prescribed at the remaining three surfaces.

The simulator is a forward model using an implicit time stepping scheme. The state of the system at a time  $t$  is evolved to a time  $t + \delta t$ , by solving the system of coupled equations using 3D finite element

methods. A dynamic time stepping scheme is adapted to capture both short and long time scale variations in field variables (typically the short time scale of the earthquakes and the long time scale of the tectonic loading). All couplings between quantities within the study are preserved by iteration procedures by solving the set of partial differential equations sequentially until convergence is achieved. The top surface is taken to be traction free. At the bottom, deformation velocity is parallel to the strike of the fault and a no tangential traction condition is imposed (Fig. 1).

## 2 MECHANO-CHEMISTRY OF EARTHQUAKE DYNAMICS

### 2.1 Incremental Stress Rheology

The strongly coupled nature of the rock deformation problem with the mechano-chemical, hydraulic and thermal processes can be captured using an incremental stress rheology. In this approach, the rate of strain is written as a sum of terms, each accounting for a particular process. It has the form (Ortoleva 1994, Tuncay *et al.* 2000a,b)

$$\dot{\epsilon}_{ij} = \dot{\epsilon}_{ij}^{pe} + \dot{\epsilon}_{ij}^{vp} + \dot{\epsilon}_{ij}^{fr} + \dot{\epsilon}_{ij}^{ps} \quad (1)$$

Here  $\dot{\epsilon}$  is the net rate of strain while the terms on the right give the contributions of poroelasticity (*pe*), viscoplasticity (*vp*), fracturing (*fr*), and pressure solution creep (*ps*).

#### 2.1.1 Poroelasticity

The rate of strain due to poroelasticity can be expressed in terms of stress, fluid pressure, and rock texture  $\Theta$  via

$$\dot{\epsilon}_{ij} = C_{ijkl}^{-1} \frac{D}{Dt} (\sigma_{ij} + \alpha(\Theta) p \delta_{ij}) \quad (2)$$

where  $\sigma$  is the total stress tensor,  $p$  is the fluid pressure,  $C$  is the fourth rank tensor of poroelasticity, and  $\alpha$  is the effective stress coefficient. Here  $D/Dt$  represents a material time derivative measuring the rate of change of a tensor in time with respect to a local reference frame fixed to a translating, rotating material volume element. The texture represents a set of variables characterizing the mineralogy, shape, size, orientation and packing of the grains of each mineral.

#### 2.1.2 Viscoplasticity

The inelastic mechanical contribution to the rate of strain is cast in the present approach as a nonlinear viscosity law in the form

$$\dot{\epsilon}_{ij}^{vp} = \eta_{ijkl} (\sigma_{ij} + p \delta_{ij}) \quad (3)$$

The fourth rank viscosity tensor depends on stress, fluid pressure, and texture.

#### 2.1.3 Fracture Formation

The dynamics of the fracture network is based on a statistical representation (Tuncay *et al.* 2000b). In our computational approach, a representative set of putative fractures of a range of orientations is introduced. The time dependent properties of each realized fracture are calculated by using the stress component normal to its fracture plane, pressure and rock properties. The volumetric strain caused by fracturing allows for a self-limiting feedback that we account for using a nonlinear incremental stress rheology. The anisotropic fracture permeability is obtained using the predicted fracture network statistics. Thus, the coupling between rock deformation, notably fracturing, and hydrology is accounted for as is that between fracturing and stress.

#### 2.1.4 Pressure Solution

A direct coupling of mechanics and chemistry arises through pressure solution. Grain dissolution at stressed grain-grain contacts induces compaction and, thereby, contributes to the total rate of strain. The rate of this pressure solution contribution depends on the stress at grain-grain contacts and, hence, on the macro-stress, fluid pressure, and composition and rock texture (Renard *et al.* 2000).

### 2.2 Conservation Equations

The Darcy law, and mass balance equations of solid phase and fluid phases, can be combined to obtain the following equation (Tuncay *et al.* 2001):

$$\phi \frac{\partial \rho}{\partial p} \frac{Dp}{Dt} + \phi \frac{\partial \rho}{\partial T} \frac{DT}{Dt} + \rho \nabla \cdot v_s = \nabla \cdot \left( \frac{k\rho}{\eta_f} (\nabla p - \rho g) \right) \quad (4)$$

where  $\phi$  is the porosity,  $k$  is the permeability tensor,  $\eta_f$  is the fluid viscosity,  $T$  is the temperature,  $v_s$  is the solid velocity. Note that  $D/Dt$  is the material time derivative with respect to the moving solid phase. The total momentum balance equation is given by

$$\sum_{j=1}^3 \frac{\partial \sigma_{ij}}{\partial x_j} + g \rho_m \delta_{i3} = 0. \quad (5)$$

where  $\rho_m$  is the bulk density of the medium. The mass balance equation for the solid phase (for incompressible grains) is

$$\frac{D\phi}{Dt} - (1 - \phi) \nabla \cdot v_s = 0 \quad (6)$$

The conservation of energy equation is given by

$$\rho_m c_{eff} \frac{DT}{Dt} + \rho_f c_f v_f \cdot \nabla T = \nabla \cdot (\lambda_{eff} \nabla T) + I \quad (7)$$

where  $c_{eff}$  and  $c_f$  are the effective and fluid heat capacity, respectively,  $\lambda_{eff}$  is the effective heat conductivity, and  $I$  is the heat source due to internal friction.

### 2.3 Friction Law

The friction expression is given by Dietrich (1979) & Ruina (1983).

$$\mu = \mu_o + a \ln(v/v_o) + b \ln(\theta/\theta_o) \quad (8)$$

where the subscript 'o' refers to the reference values at which  $\mu = \mu_o$ ,  $\mu$  is the friction coefficient, and  $a$  and  $b$  are parameters that depend on surface texture and temperature. The state variable  $\theta$  is governed by

$$\frac{d\theta}{dt} = 1 - \frac{\theta v}{d_c} \quad (9)$$

where  $d_c$  is a characteristic length.

## 3 NUMERICAL IMPLEMENTATION AND RESULTS

The simulator is a forward model using implicit time step. The state of the system at a time  $t$  is evolved to a short time later, by solving the system of coupled equations using 3D finite element methods. Equations 1-3 and 6 are solved simultaneously as described in Tuncay et al. (2000b). Another level of iteration is introduced to implement the nonlinear friction law (equations 6-8). Iterations are performed until variations in state variable and incremental deformation between two consequent iterations are smaller than specified tolerances. Fluid flow and heat flow (equations 4 and 7) are solved in separate routines. A dynamic time stepping scheme is adapted to capture both short and long time scale variations in field variables. All couplings between quantities within the study are preserved by iteration procedures by solving the equations sequentially until convergence is obtained.

Table 1. Material properties used in the simulations.

Parameter	Value	Unit
Permeability	1.0e-19	m <sup>2</sup>
Fluid Viscosity	1.0e-03	Pa.s
Bulk Modulus	20	GPa
Shear Modulus	5	GPa
Effective Stress Coefficient	1	-
Bulk Viscosity (Rock)	9.5e23	Pa.s
Shear Viscosity (Rock)	3.2e23	Pa.s
Initial Porosity	0.10	-
Heat Conductivity (Fluid)	1.88e07	J/(kg °C)
Heat Conductivity (Solid)	7.90e07	J/(kg °C)
Heat Capacity (Fluid)	4184	J/(m year)
Heat Capacity (Solid)	794	J/(m year)
Reference Fluid Density	1000	kg(m <sup>3</sup> )
Compressibility (Fluid)	0.5e-09	1/Pa
Expansivity (Fluid)	2.1e-04	1/°C

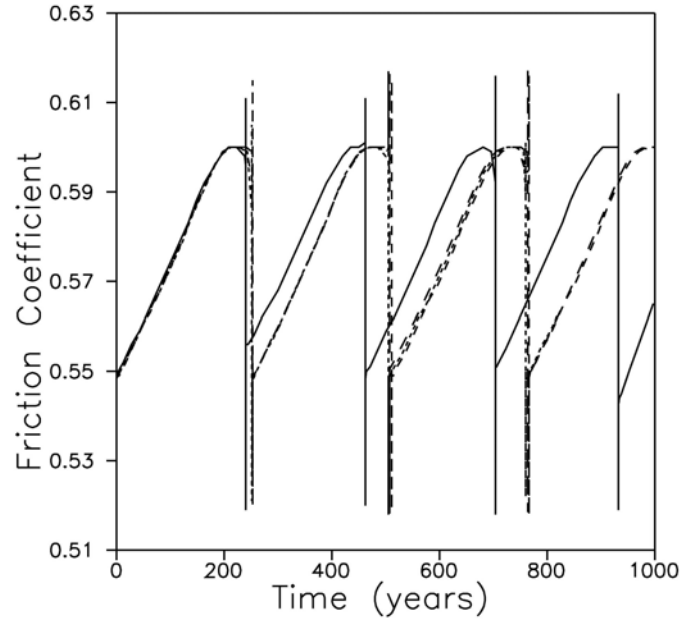


Figure 2. Friction coefficient as a function of time at the center of the fault. Results from four simulations of different finite element resolutions (20x20, 30x30, 40x40, and 50x50) are shown. The number of grids in the third dimension is kept constant at 15. The solid line is the result from the low resolution simulation (20x20). Results from the remaining three grids are practically indistinguishable from each other.

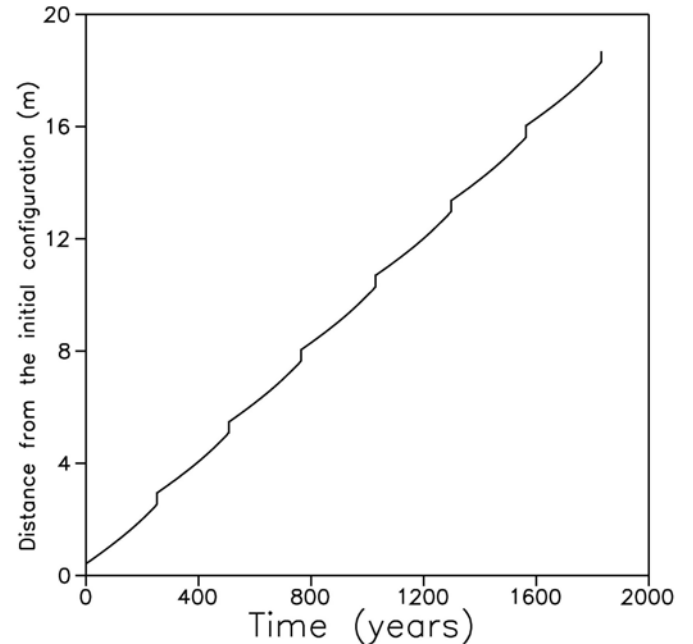


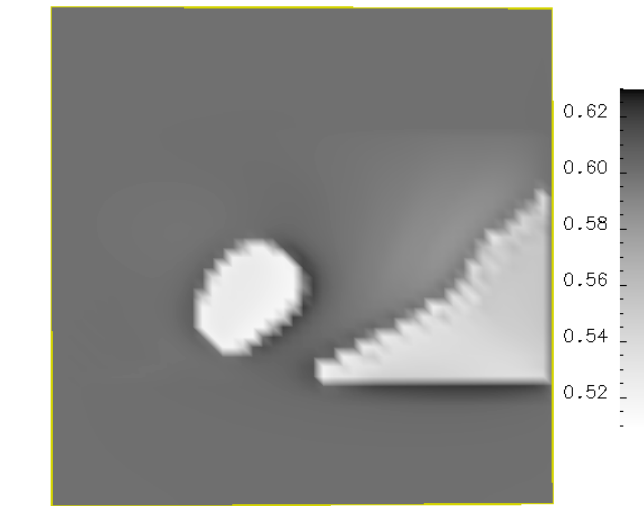
Figure 3. Distance from the initial configuration as a function of time. Each slip event is approximately 0.5 m. Note that the overall slope of the line is equal to the far field velocity (0.01 m/year).

The material properties used in the simulations are given in Table 1. The size of the system is taken to be 20 km x 20 km x 5 km (Fig. 1). At all lateral faces of the domain, a fixed velocity (0.01 m/year) is imposed. The top surface is assumed to be free of traction whereas no vertical displacement and horizontal traction conditions are imposed at the bottom. The lateral and bottom boundaries are assumed to be impermeable to fluid flow and a constant atmospheric fluid pressure condition is imposed at the sur-

face. The surface temperature is taken to be 3° C and a constant heat flux (50 mW/m<sup>2</sup>) is imposed at the bottom.

The fault surface consists of three distinct layers. The top and bottom 5 km of the fault plane is taken to be velocity-strengthening ( $a=0.005$ ,  $b=0.001$ ) whereas the middle layer is taken to be velocity-weakening ( $a=0.005$ ,  $b=0.015$ ). The reference friction coefficient  $\mu_0$  and the characteristic slip scale  $d_c$  are taken as 0.6 and 0.001 m for both velocity-weakening and velocity-strengthening layers. A viscous damping term is used to avoid unbounded slip velocities as discussed by Rice (1993). The value of the damping term is increased in an attempt to increase the time step. As noted by Rice (1993), this procedure increases the period of the seismic events.

Fig. 2 shows the evolution of the friction coefficient at the center of the fault plane for four different grid resolutions (20x20, 30x30, 40x40, and 50x50,

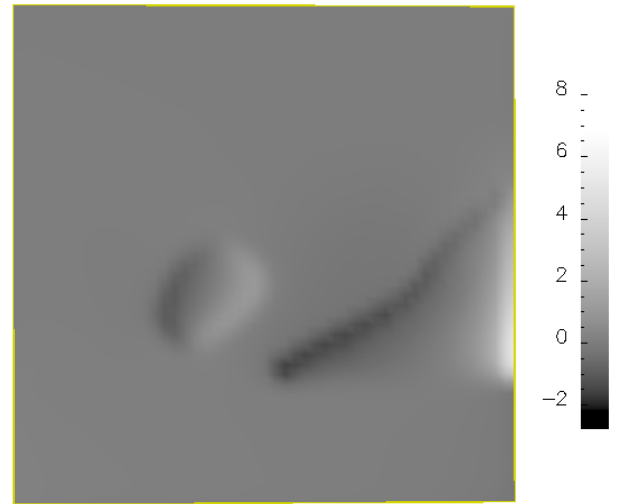


a)

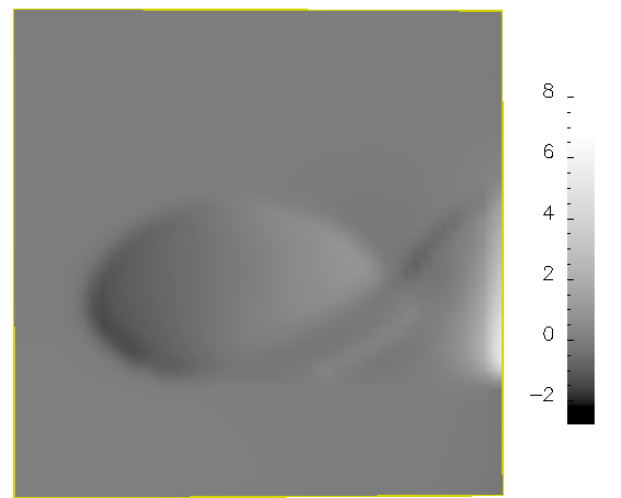


b)

Figure 4. Friction coefficient distribution on the fault plane (20 x 20 km) during a slip event. As the front propagates, the velocity difference between the sticking and slipping zones results in zones of compaction and expansion as shown in the next figure. The time lapse between frames (a) and (b) is 0.001 years.



a)



b)

Figure 5. Pressure distribution (fluctuation from the initial pressure state in MPa) on the fault plane shown during a slip event showing a pressure wave that moves along with the slip front. As pressure changes, through the effective stress principle, it effects the propagation of the slip front.

note that the number of grid elements normal to the fault plane is kept constant at 15). Except for the simulation performed with the lowest resolution, the results are practically independent of the finite element resolution, showing the consistency of our numerical approach. The slip as a function of time for the same material point is shown in Fig. 3. Each fast slip event is approximately 0.5 m and the duration of the seismic cycle is around 200 years. The shear stress drop is about 2-3 MPa.

Fig. 4 shows two snap shots of friction coefficient distribution during a fast slip event. In Fig. 4a, two separate zones of low friction coefficient are seen, whereas in Fig. 4b these zones merge as both zones continue spreading. The friction coefficient distribution in the vicinity of the borders of velocity-weakening and velocity-strengthening zones shows a sharp change. The friction coefficient increases as the slip zone tries to penetrate into the velocity-strengthening zone. During the fast slip event, there

is a significant variation of slip velocity on the fault plane. This variation results in zones of compaction and expansion at the slip fronts depending on the direction of the velocity field. In the simulations, the far field velocity is directed towards the direction of the strike of the fault, i.e, in Fig 4, the white zones (low friction) are moving to the right faster than the dark zones (high friction). Therefore one would expect expansion and compaction zones to develop on the left and right side of the low friction zone, respectively.

Fig. 5 shows the variation of fluid pressure from the initial state. The dark and light zones correspond to expansion and compaction zones, respectively. In Fig. 5a there is a circular disturbance in the pressure field that corresponds to the isolated low friction zone in Fig. 4a. As two low friction zones merge (Fig. 4b), the compaction (on the right of the circular

zone) and expansion zones collide (Fig. 5b). As pressure changes, through the effective stress principle, it affects the slip propagation.

Although, in this particular simulation, the pressure variation due to the slip event is within 10 MPa, we will now show that this variation is significant enough to change the long time scale fault behavior. In the previous simulation, rock permeability was taken to be  $1.0 \times 10^{-19} \text{ m}^2$ . In Fig. 6, results for the friction coefficient evolution from six simulations with different permeabilities are shown. At high permeabilities, the behavior is quite different than the previous simulation (Fig. 6a). The events are fairly regular and the drop in the friction coefficient is limited to 0.02. At low permeabilities, the behavior becomes less regular with friction coefficient variations as high as 0.10.

#### 4 CONCLUSIONS

Our preliminary results show that fluid flow can significantly affect long and short time scale fault motion. Our finite element formulation allows one to simulate heterogeneous systems subjected to a complex far field velocity field. Effects such as frictional heating and fluid influx to the fault system can easily be studied with our model. Permeability is shown to be an important factor in determining the fault behavior. As fault permeability during the seismic cycle changes significantly, fault models should take fracturing and fracture healing into consideration.

#### ACKNOWLEDGEMENTS

We appreciate the support of the Office of Science, U.S. Department of Energy, grant #DE-FG02-91ER14175.

#### REFERENCES

- Byerlee, J.D. 1990. Friction, overpressure and fault normal compression. *Geophysical Research Letters* 17: 2109-2112.
- Dieterich, J.H. 1979. Modeling of rock friction 1. experimental results and constitutive equations. *Journal of Geophysical Research* 84: 2161-2168.
- Hickman, S., R. Sibson, and R. Bruhn. 1995. Introduction to the special issue: mechanical involvement of fluid in faulting. *Journal of Geophysical Research* 100: 12831-12840.
- Ortoleva, P. 1994. *Geochemical Self-Organization*, Oxford University Press.
- Renard, F., Gratier, J.-P., and Jamtveit, B. 2000. Kinetics of crack-sealing, intergranular pressure solution, and compaction around active faults. *Journal of Structural Geology* 22:1395-1407.
- Rice, J.R. 1992. Fault stress states, pore pressure distributions, and the weakness of the San Andreas Fault. In *Fault Mechanics and Transport Properties in Rocks*, edited by B. Evans and T.-F. Wong, Academic Press Inc., London, 475-503.

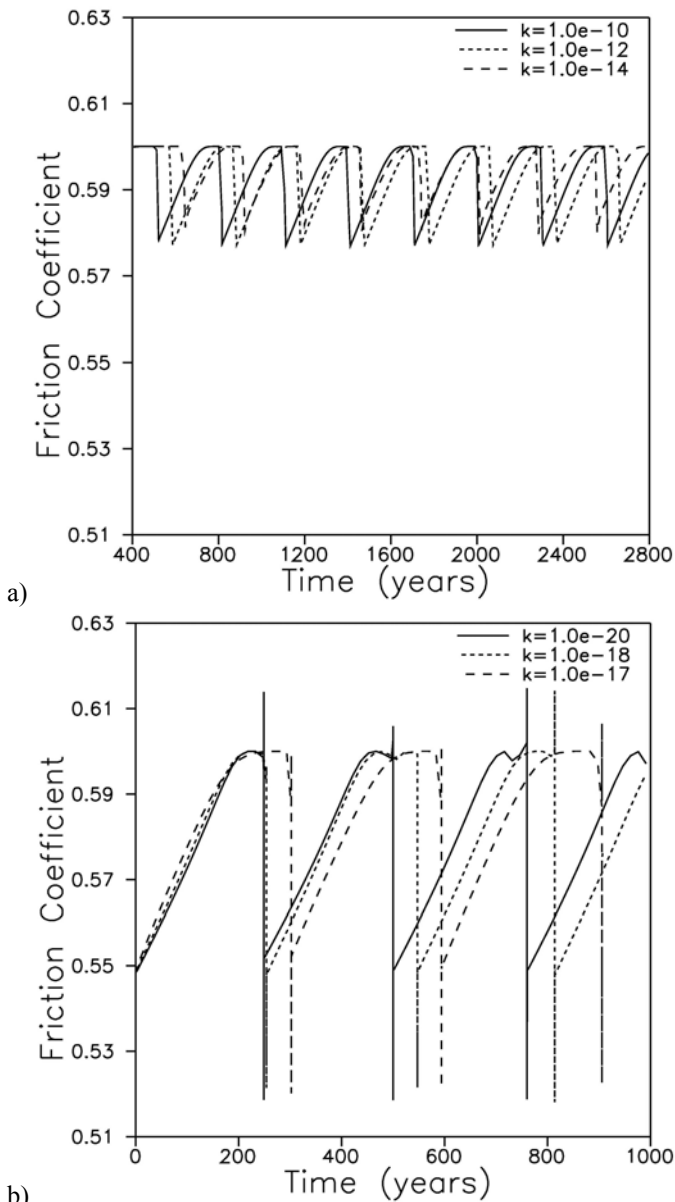


Figure 6. Effect of permeability (in  $\text{m}^2$ ) on the long time scale fault behavior. Behaviors with high permeability (a) and low permeability (b) differ significantly.

- Rice, J.R. 1993. Spatio-temporal complexity of slip on a fault. *Journal of Geophysical Research* 98: 9885-9907.
- Ruina, A. 1983. Slip instability and state variable friction laws. *Journal of Geophysical Research* 88: 10359-10370.
- Segall, P. and J.R. Rice, 1995. Dilatancy, compaction and slip instability of a fluid-infiltrated fault. *Journal of Geophysical Research* 100: 22155-22171.
- Tse, S.T., and J.R. Rice. 1986. Crustal earthquake instability in relation to the depth variation of frictional slip properties. *Journal of Geophysical Research* 91: 9452-9472.
- Tuncay, K., A. Park, and P. Ortoleva. 2000a. Sedimentary basin deformation: An incremental stress rheology approach. *Tectonophysics* 323, 77-104.
- Tuncay, K., A. Park, and P. Ortoleva. 2000b. A forward model of three-dimensional fracture orientation and characteristics. *Journal of Geophysical Research* 105:16719-16735.
- Tuncay, K., and P. Ortoleva. 2001. Salt tectonics as a self-organizing process: A three dimensional reaction, transport, and mechanics model. *Journal of Geophysical Research* 106: 803-818.
- Tuncay, K., A. Khalil, and P. Ortoleva. 2001. Failure, memory and cyclic fault movement. *Bulletin of Seismological Society of America* 91: 538-552.

# Comprehensive modeling of fault dynamics during the seismic cycle

K. Tuncay

Faculty of Earth Sciences, Utrecht University, Netherlands

F. Renard

LGIT, Université Joseph Fourier, France

P. Ortoleva

Laboratory for Computational Geodynamics, Indiana University, USA

**ABSTRACT:** A three dimensional finite element fault model that accounts for an incremental stress rheology, and fluid and heat flow is presented. In the model, mass and momentum balances for solid and fluid phases, and a total energy conservation equation are solved numerically along with a state and rate dependent friction law at the fault surface. The model allows one to study the effect of frictional heating, fluid influx from the deeper parts of faults, effect of heterogeneities on the fault behavior at the crustal scale.

## 1 INTRODUCTION

Geological evidence indicates that, in addition to the stress state and the temperature field, fluids play a key role during the seismic cycle (Hickman *et al.* 1995). After an earthquake, fractures open in the fault and in the surrounding rocks. During the interseismic period, the permeability of the fault and the country rocks tend to decrease by gouge compaction and fracture sealing. As geologic evidence is gathered on the involvement of fluids in fault dynamics, a growing number of researchers have started to study the origins and the effects of fluid pressure variations on fault mechanics (Byerlee 1990, Rice 1992, Segall and Rice 1995, Tuncay *et al.* 2001).

The goal of this study is to demonstrate how fault dynamics can be analyzed in the context of comprehensive 3D modeling at the crustal scale. We consider a rock body sliding past a rigid plate (Fig. 1). This domain represents the volume of a tectonic plate affected by a preexisting fault on its side. Our model consists of conservation of mass, momentum, and energy equations, as well as a deformation model that accounts for many deformation mechanisms, and textural evolution.

A direct coupling of mechanics and chemistry arises through pressure solution. Grain dissolution at stressed grain-grain contacts induces compaction and, thereby, contributes to overall deformation (Renard *et al.* 2000). Another coupling arises through fracture

dynamics: fractures open during a seismic event whereas fracture healing contributes to the decrease of permeability during the interseismic period. The dynamics of the fracture network is based on a statistical representation (Tuncay *et al.* 2000a). Integration of different deformation mechanisms is achieved by an incremental stress rheology (Tuncay *et al.* 2000b).

In our model we use a rate and state dependent friction law (Dieterich 1979, Ruina 1983). In this approach friction depends on velocity as well as a state variable that evolves in time. The coefficients in the

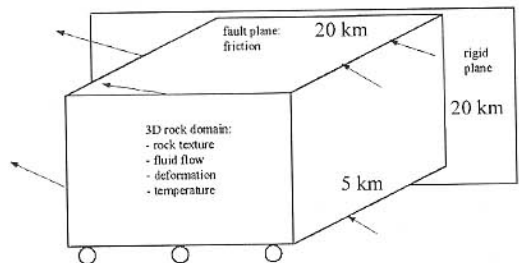


Figure 1. Schematic view of a deformable block sliding on a rigid plane. At the right-lateral slip fault plane, a state and rate dependent friction law is imposed. No vertical displacement and tangential traction are allowed at the bottom boundary. The top boundary is assumed to be traction free. The velocity field is prescribed at the remaining three surfaces.